



**HAL**  
open science

## Kinematic fields measurement during Ti-6Al-4V chip formation using new high-speed imaging system

Haythem Zouabi, Madalina Calamaz, Vincent Wagner, Olivier Cahuc, Gilles Dessein

► **To cite this version:**

Haythem Zouabi, Madalina Calamaz, Vincent Wagner, Olivier Cahuc, Gilles Dessein. Kinematic fields measurement during Ti-6Al-4V chip formation using new high-speed imaging system. International Journal of Advanced Manufacturing Technology, 2023, 10.1007/s00170-022-10575-8 . hal-03997631

**HAL Id: hal-03997631**

**<https://hal.science/hal-03997631>**

Submitted on 20 Feb 2023

**HAL** is a multi-disciplinary open access archive for the deposit and dissemination of scientific research documents, whether they are published or not. The documents may come from teaching and research institutions in France or abroad, or from public or private research centers.

L'archive ouverte pluridisciplinaire **HAL**, est destinée au dépôt et à la diffusion de documents scientifiques de niveau recherche, publiés ou non, émanant des établissements d'enseignement et de recherche français ou étrangers, des laboratoires publics ou privés.



# Kinematic fields measurement during Ti-6Al-4V chip formation using new high-speed imaging system

Haythem Zouabi<sup>1</sup> · Madalina Calamaz<sup>2</sup> · Vincent Wagner<sup>3</sup> · Olivier Cahuc<sup>1</sup> · Gilles Dessein<sup>3</sup>

Received: 31 March 2022 / Accepted: 22 November 2022

© The Author(s), under exclusive licence to Springer-Verlag London Ltd., part of Springer Nature 2023

## Abstract

Orthogonal cutting on Ti-6Al-4V produces segmented chips which results from localized deformation within the Primary Shear Zone (PSZ). For in situ visualization of the material flow during Ti-6Al-4V chip formation, a new high-speed optical system is proposed. Difficulties arise from the submillimetric size of the cutting zone. Therefore, a dedicated optical system with coaxial illumination is designed allowing for local scale analysis of chip formation. In this paper, the cutting forces were measured highlighting the unsteady nature of Ti-6Al-4V chip segmentation. For kinematic fields measurement, a novel method of Digital Image Correlation (DIC) technique is applied on the recorded images from the cutting zone. It allows for the identification of the localized deformation bands. Then, the level of the cumulative strain fields reached in the PSZ was presented and analyzed. The effect of the rake angle on the strain fields was studied. Using a 0° rake angle, the segment chip was found to be more subjected to deformation than in the case using 15°. Accuracy of the measured strain fields was discussed function of the main source of errors. In addition, the chip morphology and microstructure were investigated with a scanning electron microscopy (SEM). It shows crack opening along the PSZ and high material failure near the tool-chip interface which explains the difficulties of DIC application in the context of kinematic fields measurement during orthogonal cutting. Finally, correlation between the measured strain fields and the mean value of the chip segment width was made.

**Keywords** Chip formation · High-speed optical system · In situ measurement · Digital image correlation · Kinematic fields

## 1 Introduction

Metal cutting is a widely used process for part manufacturing. During chip formation, the material is subjected to high strain ( $>1$ ) under high strain rate that can exceed  $10^3\text{s}^{-1}$ . Understanding the mechanisms of chip formation under complex thermomechanical loads requires developing dedicated experimental set-up. In the cutting zone, the material undergoes high plastic deformation and local temperature rise that may induce changes in the material microstructure

[1, 2] as well as its mechanical and physical properties. Establishing the link between the thermomechanical load and the material microstructure evolution leads to develop physical-based models [3–6] that are suitable for numerical simulation of the machining processes. Local measurement of the displacement and strain fields in the cutting zone are with a great importance to improve the machining process. These local fields measurement can be used to predict the stress fields within the cutting zone [7, 8]. In addition, local data measurements enables to enhance/validate numerical models that could better predict the thermomechanical load at local scale [9]. Numerical simulation results are mostly compared with the experimental ones at macroscopic level [10–13] through (i) force components measurement, (ii) chip morphology and microstructure analysis and (iii) temperature measurement at the tool tip [14–17]. These quantities remain global quantities and limit the understanding of local phenomena such as strain localization [18–20]. The highly interest in understanding local phenomena during chip formation has led researchers to develop a dedicated experimental protocol allowing for in-process visualization of the material flow in the cutting zone. Indeed, two

✉ Haythem Zouabi  
haythem.zouabi@u-bordeaux.fr

<sup>1</sup> Arts et Métiers Institute of Technology, University of Bordeaux, CNRS, Bordeaux INP, INRAE, I2M Bordeaux, F-33400, Talence, France

<sup>2</sup> Arts et Métiers Institute of Technology, University of Bordeaux, CNRS, Bordeaux INP, INRAE, HESAM Université, I2M Bordeaux, F-33400, Talence, France

<sup>3</sup> Laboratoire Génie de Production, ENIT-INPT, Université de Toulouse, Toulouse, Tarbes, 65440, France

major difficulties have to be mentioned: (i) The submillimetric size of the region of interest (which disables any strain gauge to be mounted) and (ii) the rapidity of the phenomenon (which disables to retrieve in real-time the kinematic fields). First attempt to study the mechanisms of chip formation was made using Quik-Stop Devices (QSD) [21, 22]. It allows freezing the cutting process and extracting the chip root. Shear angle within the Primary Shear Zone (PSZ) could be measured. Despite the time delay for the tool-chip separation that induces errors, this technique gave results at only one instant which limits its use. An alternative technique allowing for in situ visualization of chip formation was the use of high-speed camera. Particle tracking was achieved by printing a micro-scale grid [19, 20]. High distortion of the micro-scale grid induced by the high plastic deformation within the PSZ disables a full-field displacement measurement [20].

The measurement of kinematic fields during orthogonal cutting is known to be a complex task. As the size of the cutting zone is below  $1\text{mm}^2$ , the objective that should be used must ensure magnification up to 10. Nevertheless, the depth of field decreases with the increase of magnification. The out-of-plane motion of the chip constitutes one of the main constraint. With low depth field, images captured from the cutting zone will be blurred and leads to difficulties in DIC application.

Recently, optical imaging systems have been successfully implemented for in situ measurement of kinematic fields during machining [23–27]. They offer a real-time insight on the material flow through surface observation of the workpiece. Application of the DIC technique in the context of kinematic fields measurement during orthogonal cutting has been increased these last years [28]. It allows to measure a full-field displacement with sub-pixel accuracy and to estimate the full-field strain. However, optical systems are constrained by the rapidity of physical phenomena and the out-of-plane motion of the chip ( $\pm 35\mu\text{m}$  as measured by Pottier et al. during Ti-6Al-4V chip formation under a cutting speed of 6m/min). In fact, for local scale investigation, increasing the magnification of the lens leads for low depth of field. To overcome this issue, Baizeau et al. [7] proposed the use of a telecentric  $\times 10$  finite conjugate objective. The magnification value was enough for strain field measurement within the subsurface of the workpiece. On the other hand, Calamaz et al. [29] employed a long distance microscope. The low spatial resolution of the microscope ( $3,34\mu\text{m}/\text{pixel}$ ) limits its use in the context of kinematic fields measurement within the cutting zone. Recently, Harzallah et al. [24] proposed a new optical system ensuring a better spatial resolution. Besides, illuminating submillimetric zone remains one of

the main problematics and authors did not discuss about optical solutions.

Few authors studied the evolution of the strain fields during one segment chip formation [23, 24]. This study requires a dedicated optical system for high-speed imaging of the cutting zone. Numerical post-processing of the obtained images led to determine the cumulative kinematic fields. As material in the cutting zone is subjected to high deformation, correlation between the last and the reference image (obtained from a sequence of images that describe one segment chip formation) is complicated. To overcome this issue, only Pottier et al. [23] developed a finite framework that leads to determine the cumulative displacement fields from the incremental ones measured by application of the DIC technique. The common type of correlation using the DIC technique shows its limits in the context of kinematic fields measurement during one segment chip formation.

Strain fields measured within the cutting zone helps to improve the understanding of local phenomena such as strain localization. From a mechanical standpoint, these data enable to study the effect of the cutting parameters on the strain level reached in the PSZ. Also, it can establish a link between the material deformation and the change in microstructure. Recently, these data is further used for an inverse identification of material behaviour law parameters used for finite element simulation of orthogonal cutting [9].

In this paper, a dedicated optical system was designed for in situ visualization of the material flow during orthogonal cutting. High-speed imaging of the cutting zone allows to follow the different phases of Ti-6Al-4V chip segmentation. The choice of the magnification objective is discussed. Then, a new optical solution is proposed for coaxial illumination that made possible to maximise the light intensity within submillimetric zone. In addition, it ensures uniformity in light distribution and allows to avoid under-exposure or over-exposure to light. The DIC technique was adopted for kinematic fields measurement. The application of the DIC technique is made on a sequence of images and not only 2 images. The choice of the DIC software was made so that it enables to determine the cumulative strain fields from the measured incremental ones. A novel method of DIC application was then applied and leads to directly determine the cumulative displacement and strain fields. A MATLAB script was developed for post-processing of the results returned by the DIC software. Orthogonal cutting tests were conducted on Ti-6Al-4V alloy. The experimental set-up is given. Results of the measured cutting forces are discussed. Application of the DIC technique allows to determine the kinematic fields that highlight localized shear band during Ti-6Al-4V chip formation.

## 2 Optical system

Under the camera resolution of  $512 \times 512 \text{ pixels}^2$ , an  $\times 15$  magnification objective leads to obtain an acceptable scene size allowing for in situ visualization of the material flow during chip formation. An infinity-corrected  $\times 15$  magnification objective is coupled with a 200-mm tube lens. The main reason behind choosing an infinity-corrected objective is that it enables introducing beam-splitter for coaxial illumination in the so-called infinity space delimited by the objective and the tube lens. Details of the optical system are given in Fig. 1.

The main characteristics of the optical system's components are given as follows:

- the  $\times 15$  infinity-corrected objective (1) ensures a transmittance up to 96% over the spectral band ranging between 450 and 20000 nm. This type of objective can be then used with a high-speed camera for visual imaging and also with an infrared camera for thermal inspection. The field of view of the objective is equal to  $1.2 \times 1.2 \text{ mm}^2$ .

The working distance of the objective is equal to 23.8mm. As it is a reflective objective, the transmission of the emitted radiations is made by double reflection by mean of two mirrors (Fig. 2).

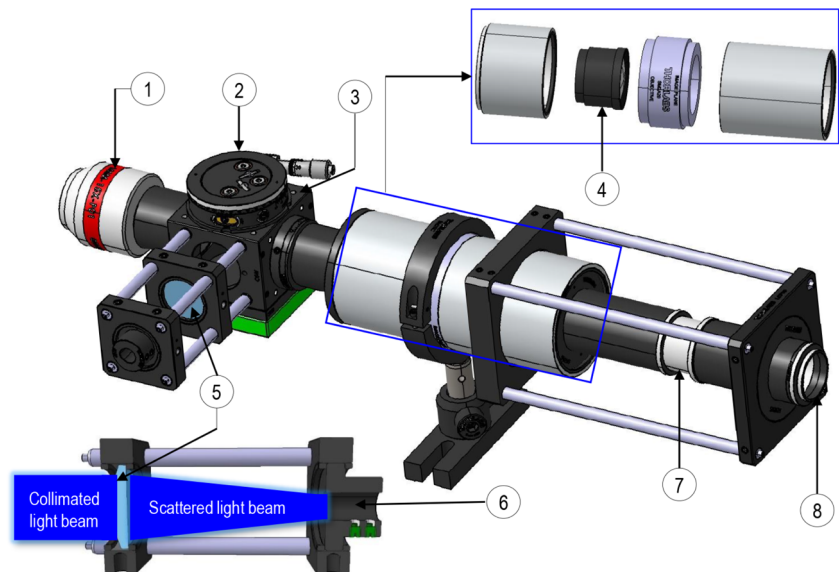
- the rotating platform (2) is used to adjust a beam-splitter at  $45^\circ$  with respect to the optical axis. This beam-splitter ensures a 50% of reflectance and a 50% of transmittance in the spectral band ranging between 400 and 700 nm. Both the rotating platform and the beam-splitter are mounted in a 30-mm cube cage.
- Cold light source of 150W is used for illumination. The collimated light beam is obtained by mean of the f60mm plano-convex lens (5). It features an AntiReflective (AR) coating for the spectral band ranging between 350 and 700 nm (Fig. 3) which reduces the reflectance down to 3%.

This new optical solution allows to maximize the light intensity while illuminating submillimetric zone. Using a reflective objective (Fig. 2), the light will be focalized on the field of view.

Compared to classical technique of illumination using a collimator or a focalizer (Fig. 4.a), coaxial illumination (Fig. 4.b), combined with a reflective objective, allows to reduce the obscure band. Therefore, the integration time can be reduced to  $14 \mu\text{s}$  which allows to reach a relatively high cutting speed of 40m/min. As a result, the obtained images are unblurred and well exposed to light.

- the tube lens (4) with a focal length equal to 200mm is used allowing to keep the magnification of the

**Fig. 1** New high-speed imaging system dedicated for kinematic fields measurement during orthogonal cutting



1	X15 infinity corrected objective	5	F60mm plano-convex lens
2	Rotating platform	6	Fiber optic housing
3	30mm cube cage	7	SM1 coupler
4	200mm tube lens	8	C-mount adapter

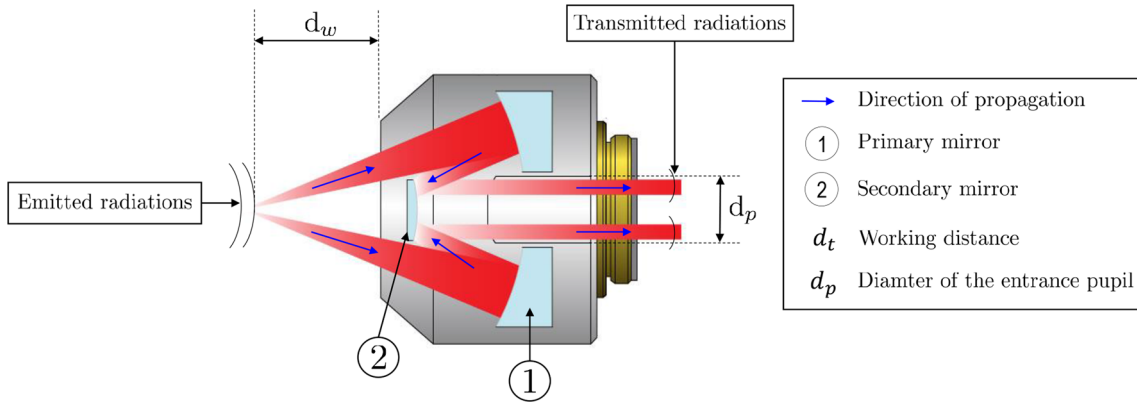


Fig. 2 Schematic illustration of the principle of transmission by double reflection of a reflective objective

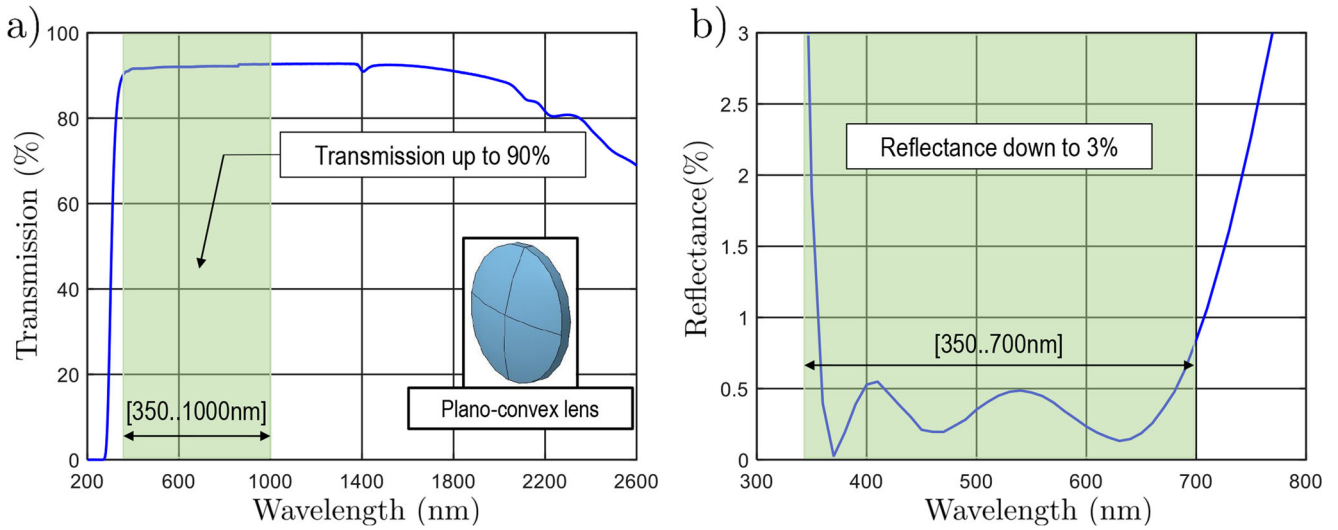


Fig. 3 Percentage of a) transmission and b) reflectance of a plano-convex lens with an AntiReflective coating (Data obtained from Thorlabs)

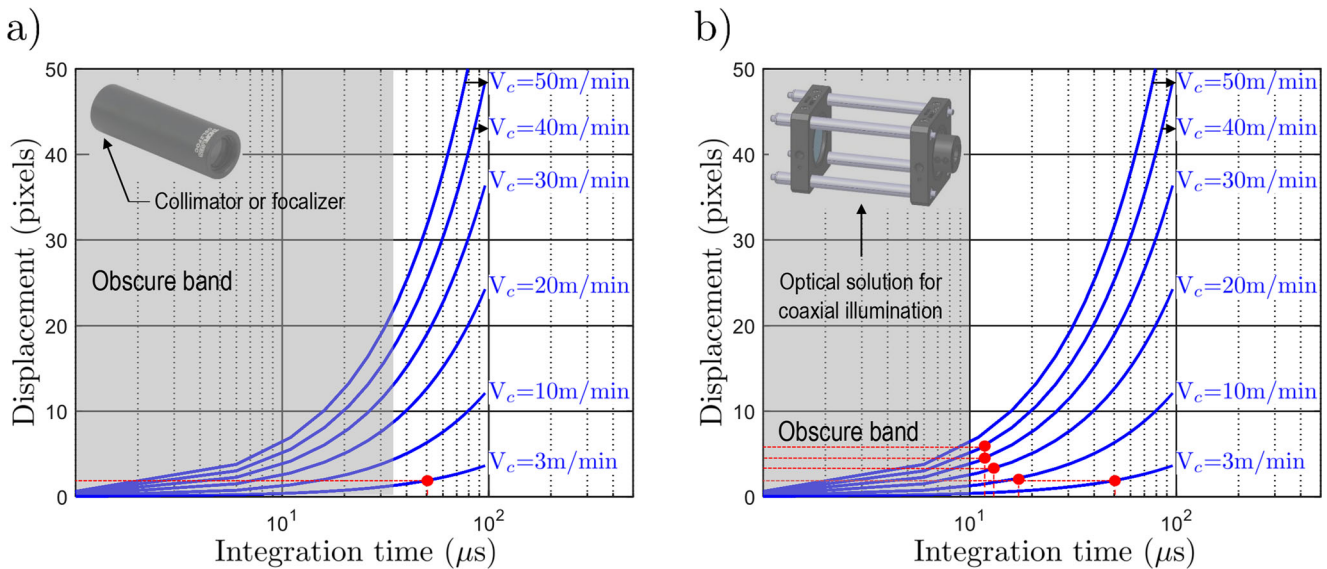


Fig. 4 Displacement of the observed scene function of the integration time and the cutting speed: a) when using a collimator or a focalizer and b) the optical solution for coaxial illumination

objective at  $\times 15$ . It ensures a transmittance up to 90% in the visible spectrum band. The distance that should separate the tube lens from the sensor array of the high-speed camera is equal to 148 mm. For that, an SM1 coupler (7) is used for adjustment.

- the C-mount adapter (8) is used to connect the optical system with high-speed camera.

This optical system was designed specifically for high-speed imaging of the cutting zone. It allows to follow the different phases of Ti-6Al-4V chip segmentation. By application of the DIC technique on the recorded images, the kinematic fields are measured. Thus, the mechanisms of chip formation during orthogonal cutting on Ti-6Al-4V are analyzed from the measured displacements and strains fields at local scale.

### 3 Digital image correlation

In this paper, the DIC technique was used for kinematic fields measurement during Ti-6Al-4V chip formation. Indeed, it ensures enough spatial resolution for localized shear band identification. A novel method of DIC is applied allowing to measure the cumulative kinematic fields. Basically, the most used types of correlation are as follows: (i) Incremental (Inc.) and (ii) Non Incremental (Non-Inc.) (Fig. 5a). However, they can not be recommended for high strain fields measurements. In orthogonal cutting, material in the cutting zone is subjected to high strain. In addition, illumination can not be kept constant as the chip undergoes an out-of-plane motion. Both lead to difficulties in DIC application on a sequences of images that describes the different phases of segmented chip formation. Based on the update of the region of interest (ROI) at each increment, the cumulative kinematic fields are measured form incremental correlation (Fig. 5.b).

A classification of different DIC softwares is made in order to verify mainly the existence of the IC2KF method (Table 1) that it is suitable in the context of kinematic fields measurement during orthogonal cutting. From Table 1, only Ncorr DIC software allows for the IC2KF method.

To evaluate the similarity between a given subset in the reference image and the corresponding one in the deformed image, a correlation criterion should be introduced. In this work, a ZNSSD correlation criterion is used with Ncorr:

$$C_{ZNSSD} = \sum_{i=-M}^M \sum_{j=-M}^M \left[ \frac{f(X_i, Y_j) - f_m}{\Delta f} - \frac{g(x_i, y_j) - g_m}{\Delta g} \right]^2 \quad (1)$$

where  $f(X_i, Y_j)$  is the gray level at pixel in the position  $(X_i, Y_j)$  in the reference image;  $g(x_i, y_j)$  is the gray level

of the corresponding pixel in the deformed image;  $2M+1$  is the size of the subset centered at  $(X_0, Y_0)$  (respectively  $(x_0, y_0)$ ) in the reference image (respectively in the deformed image) and:

$$\begin{cases} f_m = \frac{1}{(2M+1)^2} \sum_{i=-M}^M \sum_{j=-M}^M f(X_i, Y_j) \\ g_m = \frac{1}{(2M+1)^2} \sum_{i=-M}^M \sum_{j=-M}^M g(x_i, y_j) \end{cases} \quad (2)$$

$$\begin{cases} \Delta f = \sqrt{\sum_{i=-M}^M \sum_{j=-M}^M [f(X_i, Y_j) - f_m]^2} \\ \Delta g = \sqrt{\sum_{i=-M}^M \sum_{j=-M}^M [g(x_i, y_j) - g_m]^2} \end{cases} \quad (3)$$

This correlation criterion ensures no sensitivity to both offset and linear scale in lighting [33] and indicates good match when  $C_{ZNSSD}$  is close to 0 (Fig. 6). In the reference image, the displacement components of each point  $(X_i, Y_j)$  are denoted by  $(U_{X_i}, U_{Y_j})$ .  $U_{X_i}$  (respectively  $U_{Y_j}$ ) is the displacement along the  $x$ -axis (respectively along  $y$ -axis). In the deformed image, the displacement components of each material points  $(x_i, y_j)$  are denoted by  $(U_{x_i}, U_{y_j})$ .

- **Eulerian configuration** In this paper, Eulerian configuration was adopted so that the measured strain fields can be interpreted from the deformed images. In fact, when using Eulerian configuration, the cumulative strain fields are given in the current (or the deformed image). The components of the Eulerian-Almansi strain tensor computed from the displacement gradients are given by:

$$\begin{cases} A_{xx} = \frac{1}{2} [2 \frac{\partial U_x}{\partial x} - (\frac{\partial U_x}{\partial x})^2 - (\frac{\partial U_y}{\partial x})^2] \\ A_{xy} = \frac{1}{2} [\frac{\partial U_x}{\partial y} + \frac{\partial U_y}{\partial x} - \frac{\partial U_x}{\partial x} \frac{\partial U_x}{\partial y} + \frac{\partial U_y}{\partial x} \frac{\partial U_y}{\partial y}] \\ A_{yy} = \frac{1}{2} [2 \frac{\partial U_y}{\partial y} - (\frac{\partial U_x}{\partial y})^2 - (\frac{\partial U_y}{\partial y})^2] \end{cases} \quad (4)$$

Direct differentiation of the displacement field is sensitive to noise. This means that noise in the measured displacement field leads to errors in the strain field obtained by direct differentiation. In order to overcome this issue, Ncorr DIC software [32] uses a least squares plane fit on the displacement data within a strain calculation window of a given radius (Fig. 7) to determine the displacement gradients:

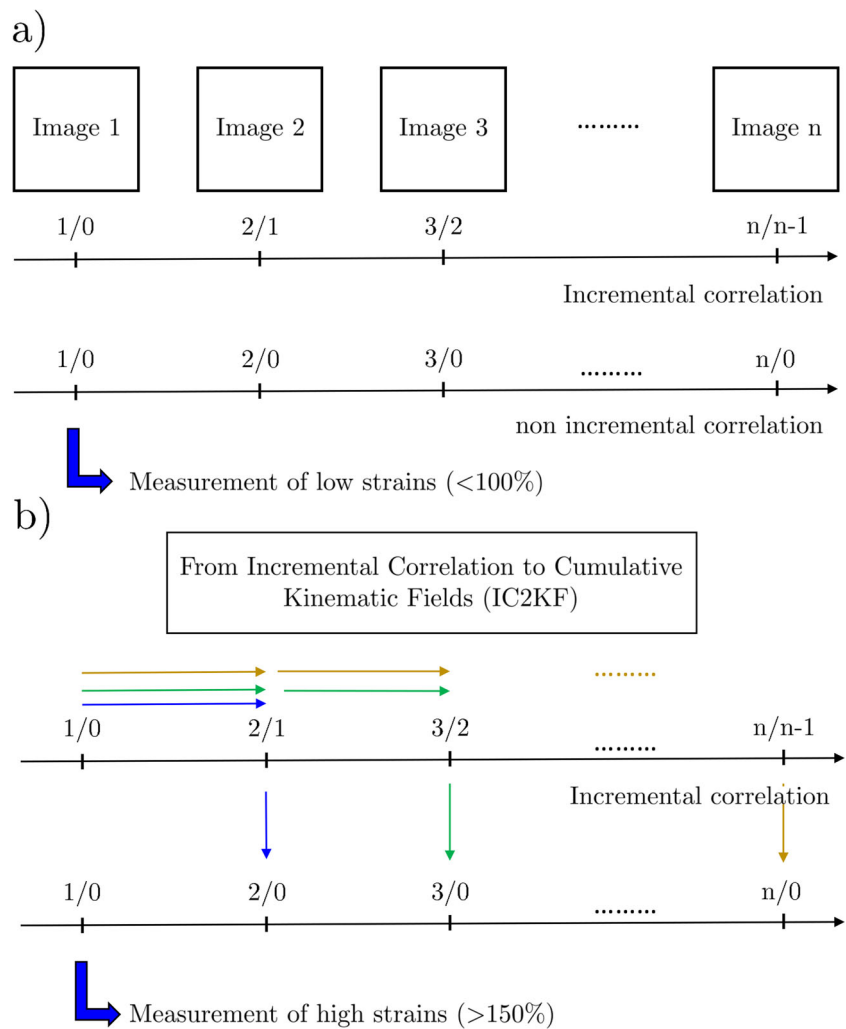
$$\begin{cases} U_{x,plane}(x, y) = a_{U_{x,plane}} + (\frac{\partial U_x}{\partial x})x + (\frac{\partial U_x}{\partial y})y \\ U_{y,plane}(x, y) = a_{U_{y,plane}} + (\frac{\partial U_y}{\partial x})x + (\frac{\partial U_y}{\partial y})y \end{cases} \quad (5)$$

where  $(U_{x,plane}, U_{y,plane})$  are the displacement components obtained by the least squares plane fit and  $(a_{U_{x,plane}}, a_{U_{y,plane}})$  are the parameters of the fitting.

Principal strains,  $A_M$  and  $A_m$  where  $A_M$  (respectively  $A_m$ ) denotes the major strain (respectively the minor strain) are defined as the eigenvalues of the strain tensor:

$$\begin{cases} A_M = \frac{A_{xx} + A_{yy}}{2} + \frac{1}{2} \sqrt{(A_{xx} - A_{yy})^2 + 4A_{xy}^2} \\ A_m = \frac{A_{xx} + A_{yy}}{2} - \frac{1}{2} \sqrt{(A_{xx} - A_{yy})^2 + 4A_{xy}^2} \end{cases} \quad (6)$$

**Fig. 5** a) Incremental and non incremental correlation and b) from incremental correlation to cumulative kinematic fields (IC2KF)



The equivalent strain is then given by:

$$A_{eq} = \sqrt{\frac{2}{3}(A_M^2 + A_m^2)} \quad (7)$$

A MATLAB script (Fig. 8) was developed to convert the displacement fields from pixel to micron unit. In addition, it is used to compute the minor, the major and the equivalent strain fields. Knowing the image size, this script allows to

superimpose all the measured fields (displacement, strain and equivalent strain fields) on visual images captured by the high-speed camera. In this paper, DIC technique is applied on the recorded images of one segment chip for kinematic fields measurement. The effect of the rake angle is examined through the results of the measured strain fields. Comparison between the equivalent strain reached within the localized shear band in the case using 0° and 15° rake angle is made.

**Table 1** Classification of different DIC softwares

DIC software	Correlation criterion	Correlation type	Approach	IC2KF
Correli Q4 [30]	SSD <sup>1</sup>	Inc. and Non-Inc.	Global	<b>X</b>
VIC 2D	SSD, NSSD <sup>2</sup> and ZNSSD <sup>3</sup>	Inc. and Non-Inc.	Local	<b>X</b>
7D [31]	NCC <sup>4</sup> and ZNCC <sup>5</sup>	Inc. and Non-Inc.	Local	<b>X</b>
Ncorr [32]	ZNSSD	Inc.	Local	<b>+</b>

<sup>1</sup>SSD: sum of squared differences

<sup>2</sup>NSSD: normalized sum of squared differences

<sup>3</sup>ZNSSD: zero normalized sum of squared differences

<sup>4</sup>NCC: normalized cross-correlation

<sup>5</sup>ZNCC: zero normalized cross-correlation

Inc (incremental)

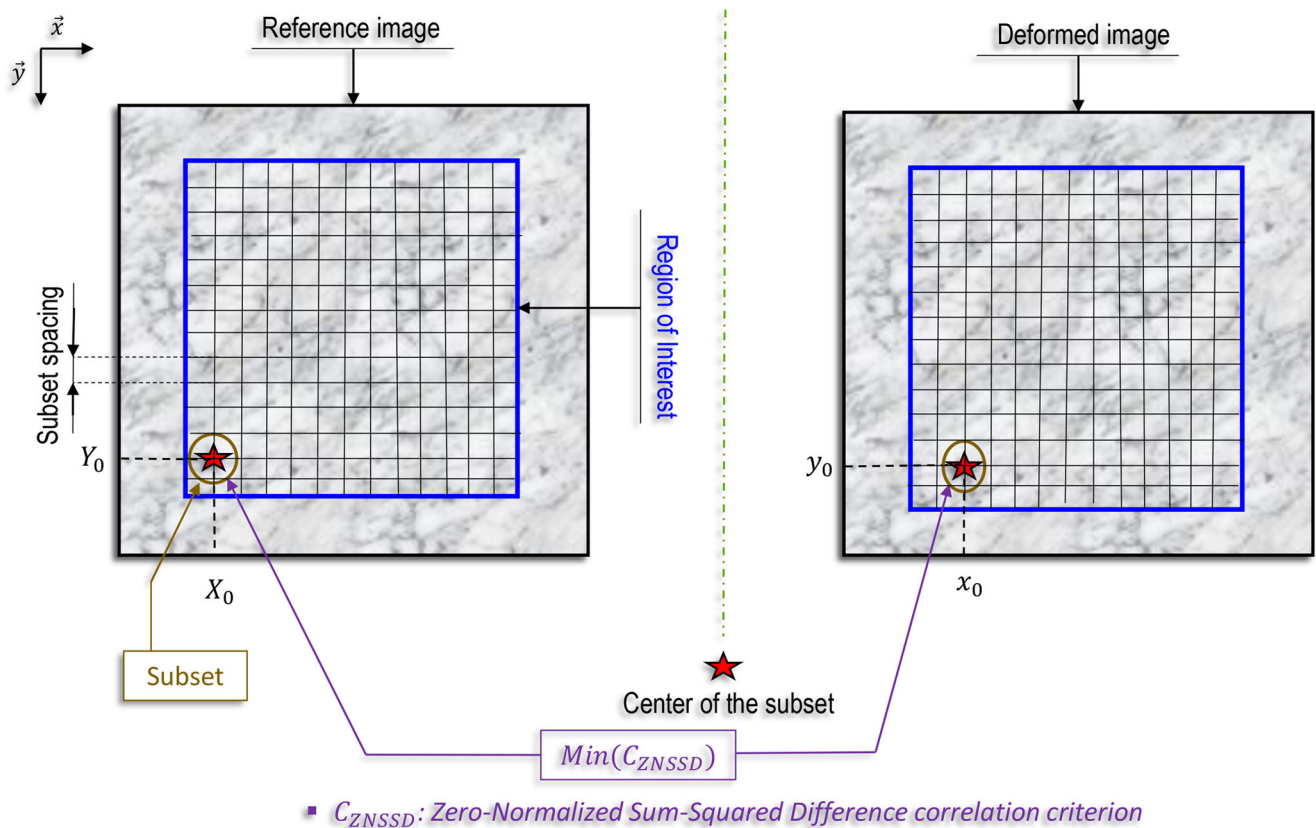


Fig. 6 Illustration of the subset matching using the DIC technique with local approach

### 4 Experimental set-up

Orthogonal cutting tests are made on rectangular Ti-6Al-4V workpiece under a cutting speed  $V_c=3\text{m/min}$  and a

feed  $a=0,2\text{mm}$ . The width of cut is equal to 3mm. The workpiece surface side (Fig. 9) was polished and etched using a Kroll solution in order to reveal the material microstructure considered as a natural speckle for particle

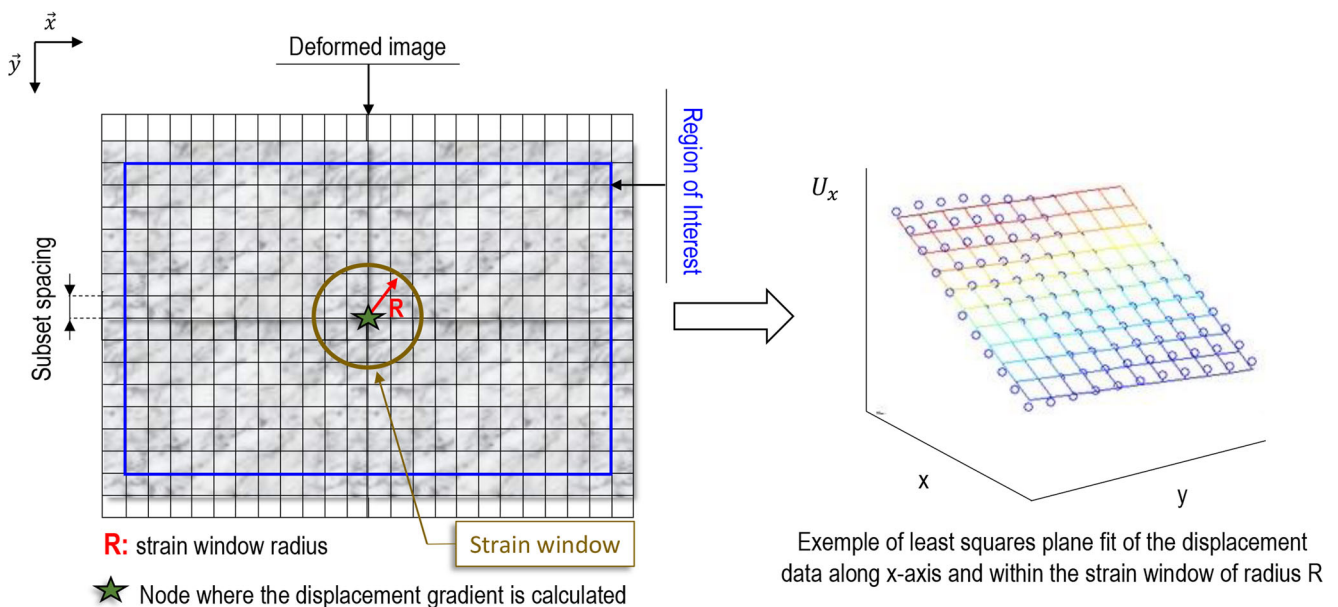
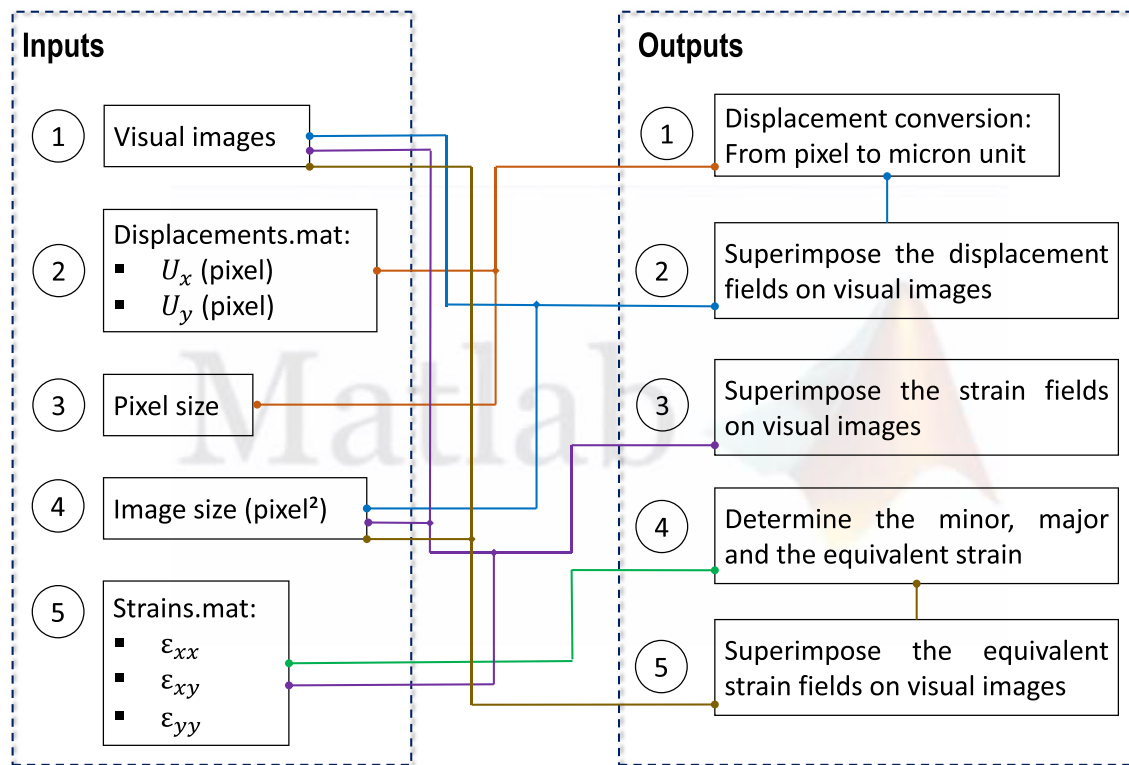


Fig. 7 Illustration of the least squares plane fit on the displacement data to determine the displacement gradient



**Fig. 8** Description of the developed script: inputs, outputs and links

tracking. An equiaxed microstructure composed of  $\alpha$  and  $\beta$  phases is observed with an SEM view (Fig. 9c) In this work, a new experimental bench (Fig. 10) was designed to ensure high rigidity over hard-to-cut materials such as titanium and Inconel alloys and more precision in kinematic fields measurement. Orthogonal cutting tests are made by translation of the workpiece in front of a fixed cutting tool. Low cutting speed was chosen in order to validate the new high-speed optical system. Moreover, the adjustment of the optical parameters under 3m/min leads to obtain contrasted images that is suitable for DIC application as first-conducted test on Ti-6Al-4V alloy. H13A uncoated carbide cutting inserts were used. The first test was made with a rake angle of  $0^\circ$  while the second one was with  $15^\circ$  rake angle. The clearance angle in both tests was equal to  $11^\circ$ . Perpendicularity of the workpiece surface with respect to the tool rake face was adjusted to (0,  $+10\ \mu\text{m}$ ). Figure 11 gives the experimental set-up used for high-speed imaging of the cutting zone.

**Cutting forces** Kistler 9129AA dynamometer was used for the cutting efforts measurements.  $F_c$  denotes the cutting force (along  $x$ -axis) and  $F_f$  is the feed force (along  $y$ -axis). The acquisition frequency was set to 20000 Hz. Figure 12 gives the evolution of the cutting forces. The mean values as well as the maximum and the minimum of the measured forces are summarized in Table 2. Under the same

cutting speed,  $F_c$  and  $F_f$  decrease when the tool rake angle increases.

From Fig. 12, an unsteady fluctuation of the cutting efforts can be observed. Figure 13 shows the periodicity of Ti-6Al-4V chip segmentation function of the cutting parameters. Three different domains are identified from microscopic view made on the collected chips: (i) aperiodic segmentation, (ii) transition phase and (iii) quasi-periodic segmentation. The cutting parameters of  $a=0.2\text{mm}$ ,  $V_c \leq 10\text{m/min}$  and both rake angle (Fig. 13a and b) belong to the domain of the aperiodic segmentation which explains the unsteady fluctuation of the cutting efforts (Fig. 12).

## 5 Results and discussion

The mechanisms of segmented chip formation can be described with 3 phases (Fig. 13):

- Phase 1: the material near the tool tip starts to deform under a significant compression along  $X$ -axis. During this phase, an out-of-plane motion of the segment chip will occur [23]. It can be attributed mainly to the deformation along  $Y$ -axis. However, the magnitude of this deformation can be neglected with the assumption of plane deformation.

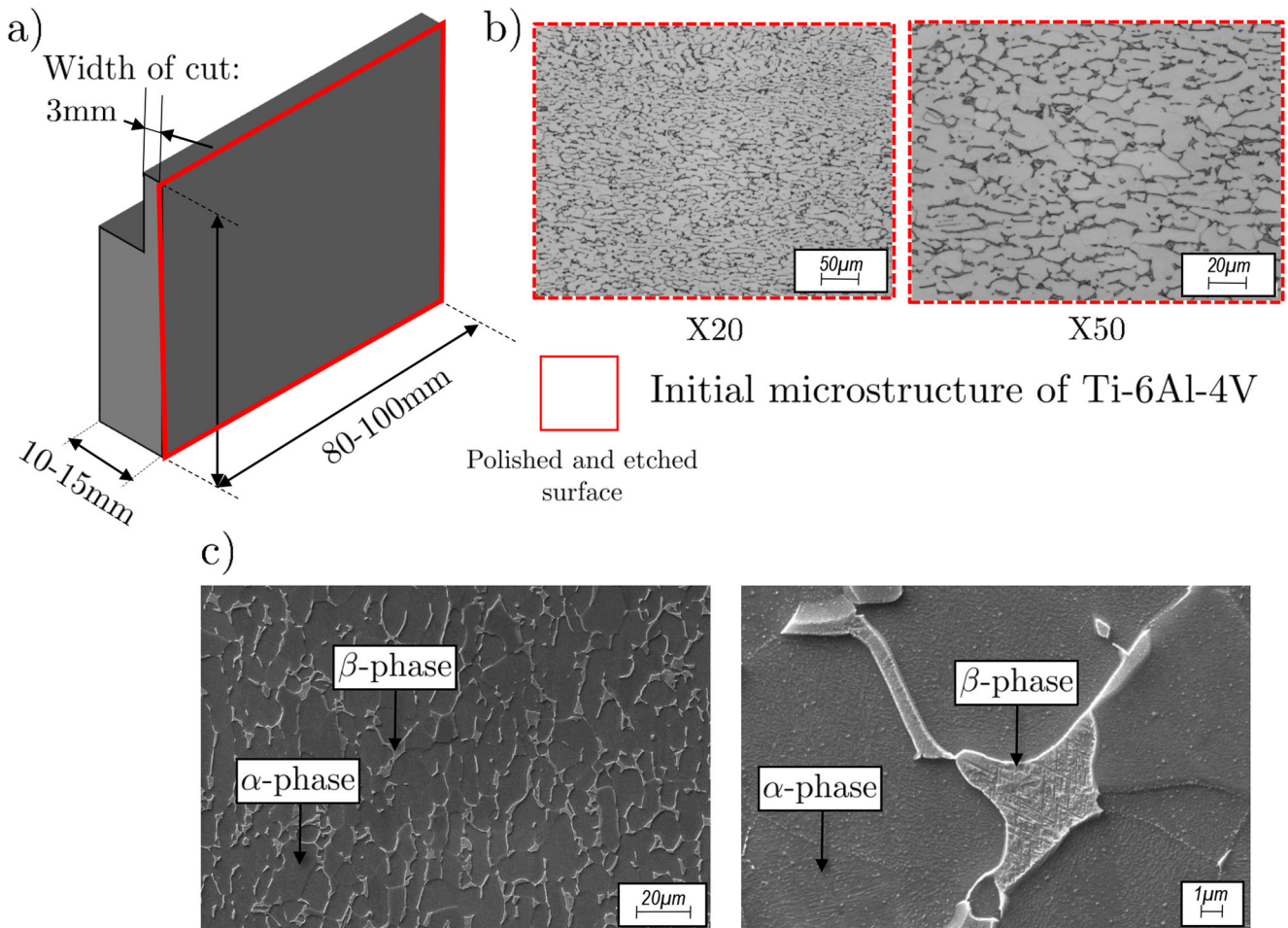
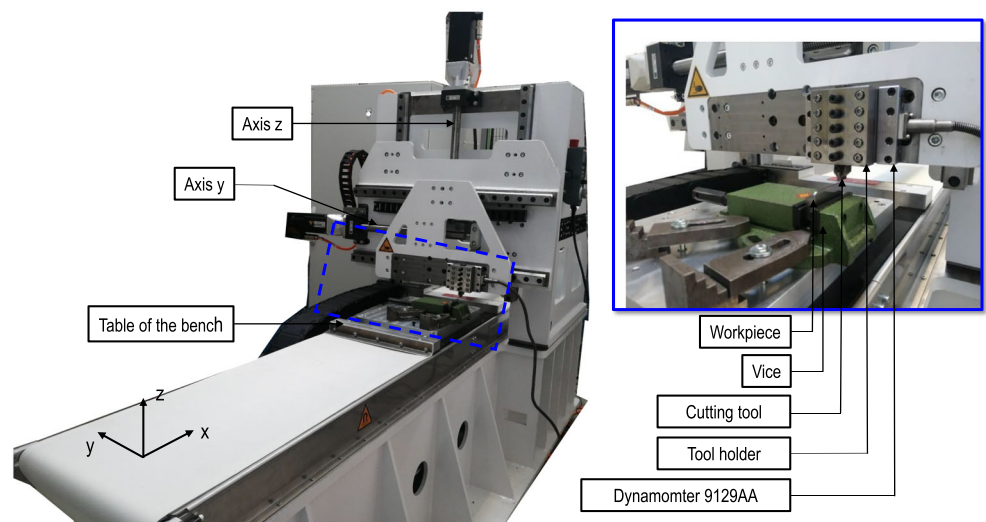


Fig. 9 a) Geometry of the workpiece, b) Ti-6Al-4V initial microstructure and c) SEM view and the existing phases

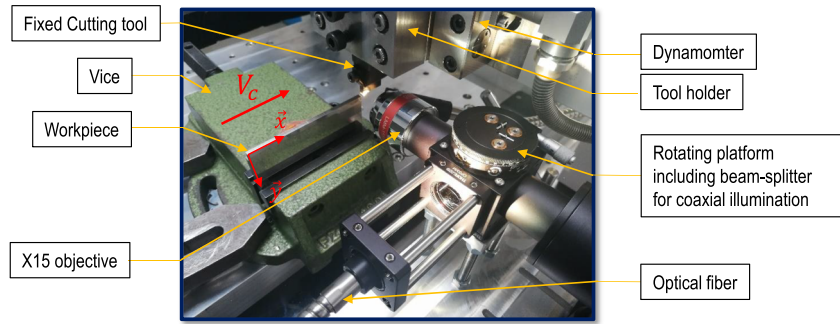
- Phase 2: the localized deformation near the tool tip starts to propagate towards the free surface of the workpiece along the adiabatic shear band (ASB). An intense shear is occurred and reach

- the point of the material failure. This will initiate a crack that starts to propagate along the ASB.
- Phase 3: The crack is fully formed. The ejection of the segment chip is made by sliding with

Fig. 10 New experimental bench used for instrumented orthogonal cutting tests



**Fig. 11** Experimental set-up for high-speed imaging of the cutting zone



respect to the shear plane under the assumption of rigid body motion. With the movement of the workpiece, the segment chip will further slide with respect to the tool rake face. The out-of-plane motion of the segment chip is more pronounced in this phase.

This description remains phenomenological and limits the comprehension of the mechanisms of segmented chip formation. Quantitative data giving the level of strain reached in the ASB helps to study the effect of the cutting parameters on the material deformation within the cutting zone. Thus, it enhances the comprehension of the segment chip formation from a mechanical standpoint.

### 5.1 Kinematic fields measurement

- **Optical parameters** The camera resolution of the Fastcam APX-RS high-speed camera was set to

$$n = \frac{f_{aq} \times a}{V_c} \tag{8}$$

512×512pixels. This yields to obtain a scene size of 0.58×0.58mm<sup>2</sup> allowing for in situ visualization of the material flow during Ti-6Al-4V segment chip formation. The pixel size is theoretically equal to 1.13μm/pixel. It was adopted for the displacement field conversion from pixel to micron unit. The integration time was chosen so that it reduces the blur induced by the scene displacement. Setting a maximum of 2.21pixels displacement, the corresponding integration time is equal to 50μs. Assuming that the speed of chip motion is equal to the cutting speed and the segment width is equal to the feed [23], the number of images per one segment chip (n) function of frame rate (f<sub>aq</sub>) can be predicted. Using 10000 fps with a cutting speed of 3m/min and a feed of 0.2 mm, theoretically 40 images per one segment chip can be obtained (8 for calculation).

**Fig. 12** The measured cutting efforts under V<sub>c</sub>=3m/min: a) γ=0° and b) γ=15°

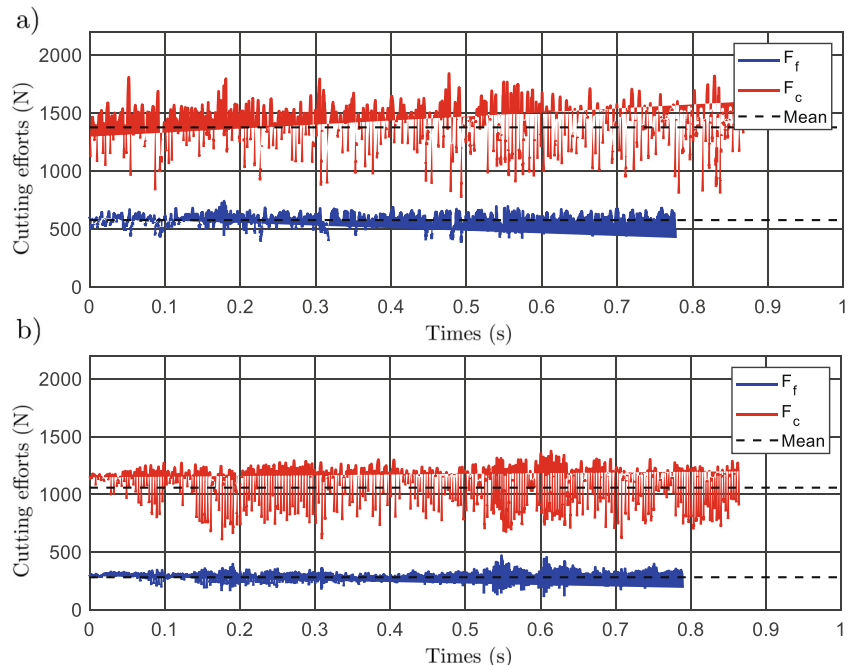


**Table 2** Mean, maximum and minimum values of the measured cutting efforts

Test n°	$F_{f,mean}$ (N)	$F_{c,mean}$ (N)
Test 1 ( $V_c=3\text{m/min}$ ; $\gamma=0^\circ$ )	577 (max:851/ min: 306) Std <sup>1</sup> (N): $\pm 51$	1377 (max:1841/ min: 701) Std (N): $\pm 166$
Test 2 ( $V_c=3\text{m/min}$ ; $\gamma=15^\circ$ )	282 (max: 469/ min: 110) Std (N): $\pm 31$	1058 (max: 1375/ min: 591) Std (N): $\pm 141$

<sup>1</sup>Std: the standard deviation of the mean value of the cutting component

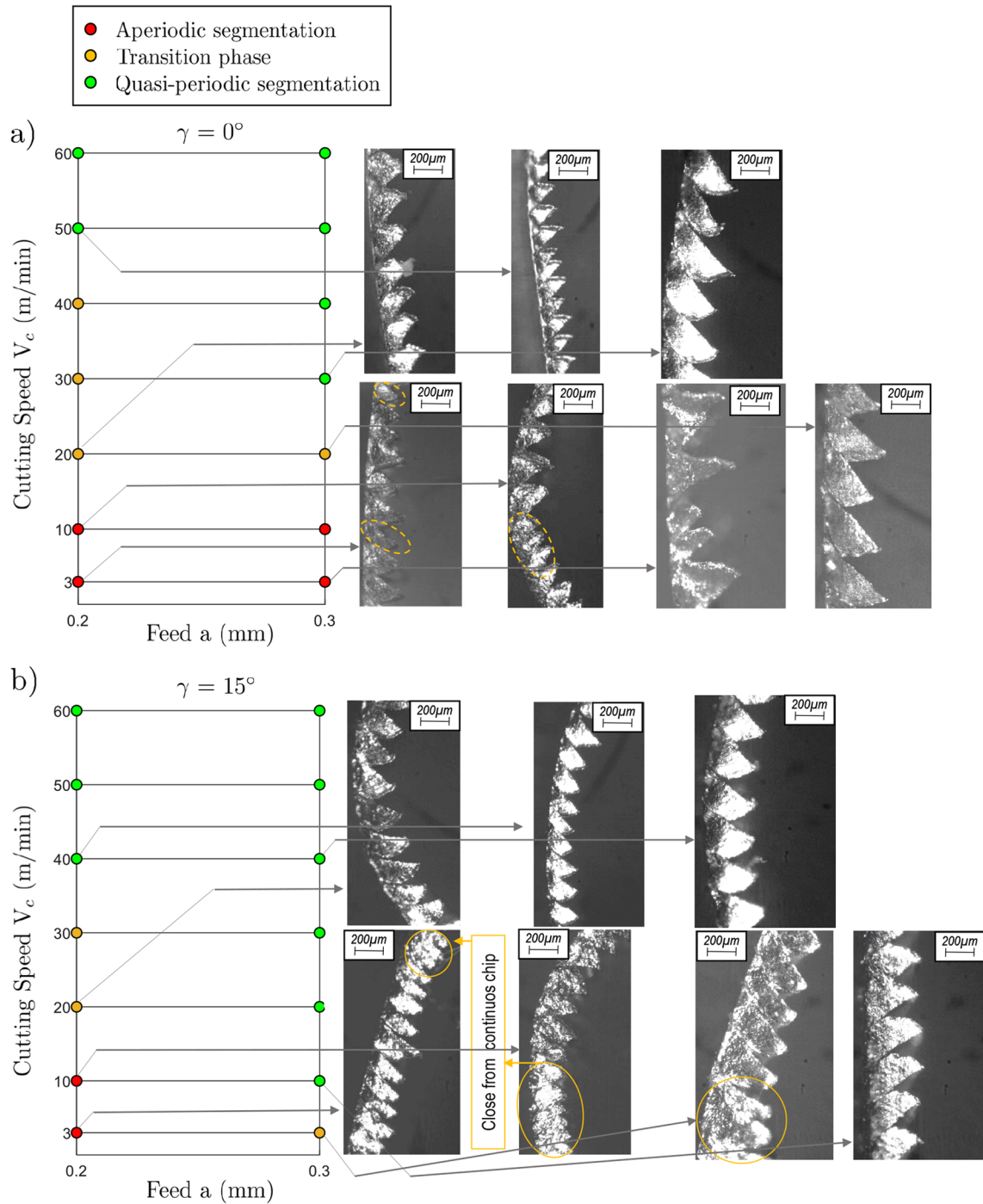


**Fig. 13** Periodicity of Ti-6Al-4V chip segmentation function of the cutting speed and the feed under: a)  $\gamma=0^\circ$  and b)  $\gamma=15^\circ$

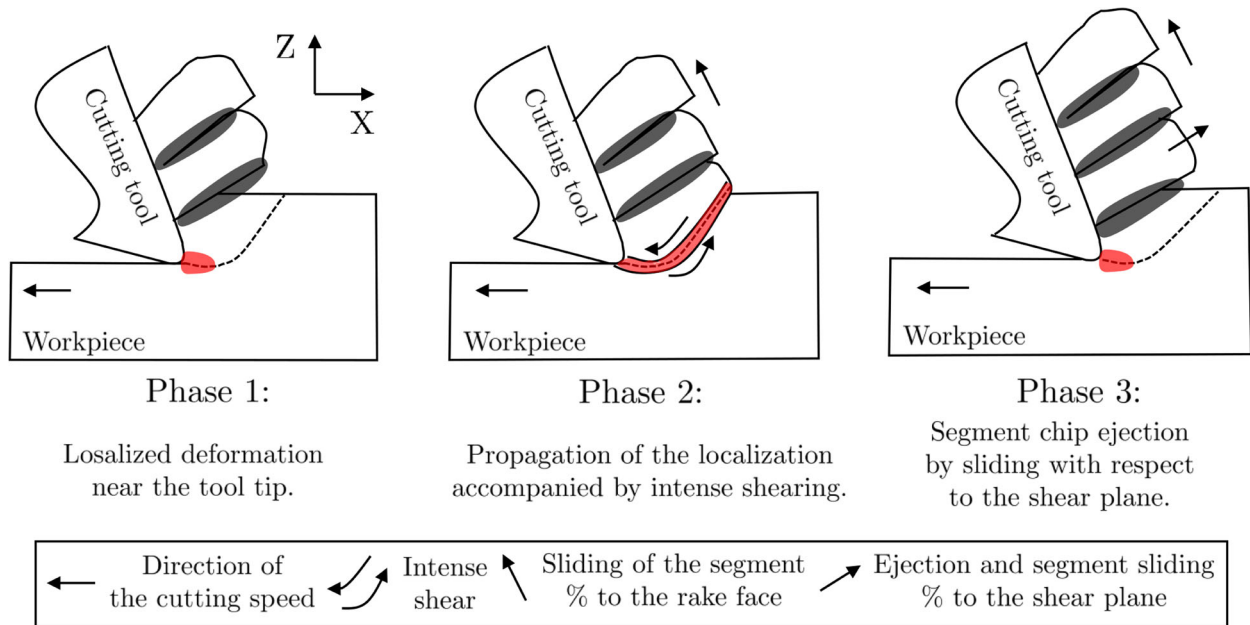
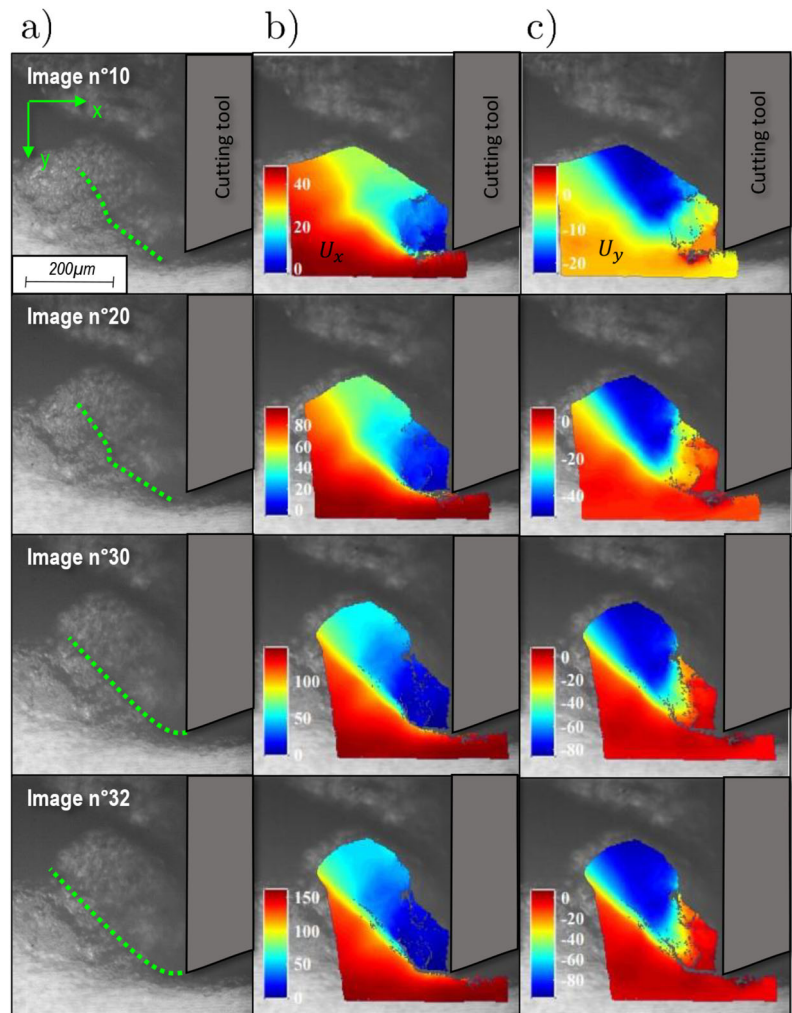


Fig. 14 Mechanisms of segmented chip formation

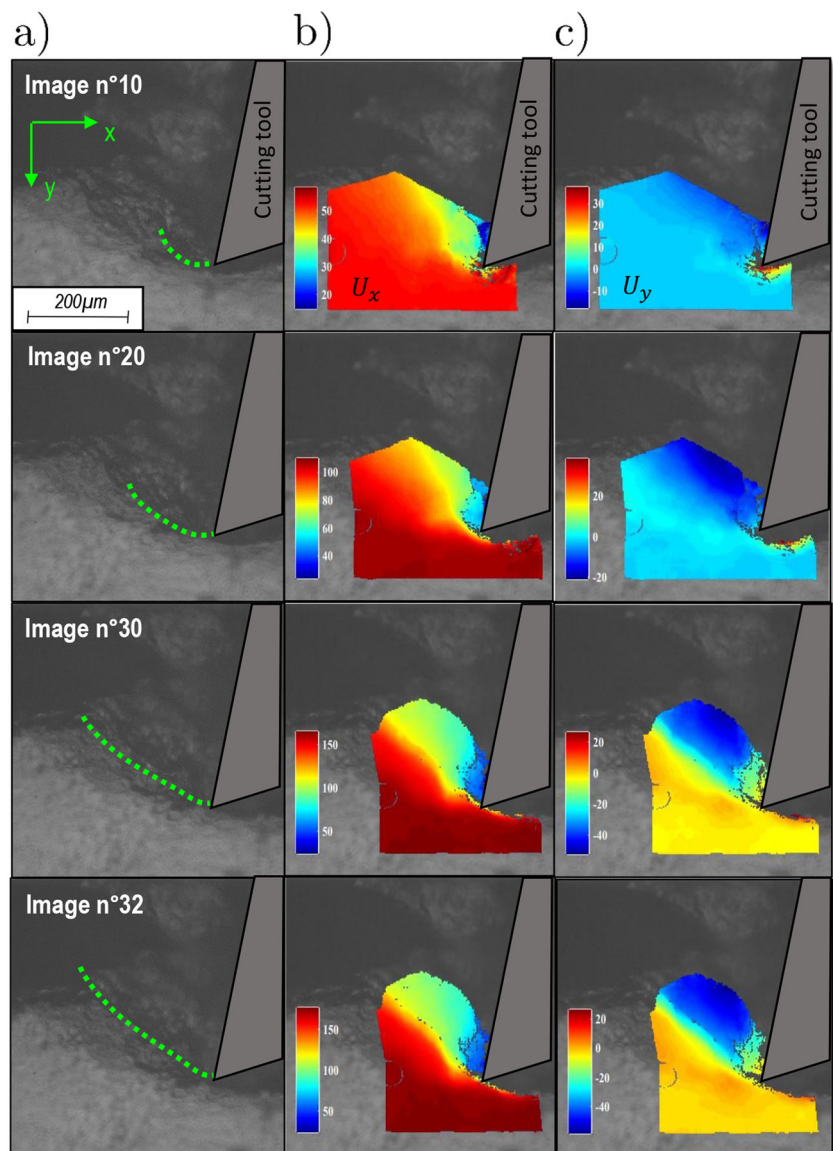
Fig. 15 a) Visual images obtained during Ti-6Al-4V segment chip formation under  $V_c=3\text{m/min}$  and  $\gamma=0^\circ$ ; b) displacement field along  $x$ -axis ( $U_x$ ) and c) displacement field along  $y$ -axis ( $U_y$ )



- **DIC parameters** Digital image correlation was applied on the recorded images from the cutting zone during chip formation. Ncorr DIC software using a local approach was used [32]. The region of interest (ROI) was discretized into circular subset with a radius of 25pixels. The subset spacing as defined with the DIC software was set to 1pixel. This means that the distance separating two consecutive nodes is equal to 2pixels (1+subset spacing). For the strain calculation, a window with a radius of 5pixels was adopted.
- **Results of kinematic fields measurement** Digital image correlation was applied on 34 images (respectively on 33 images) for the test made with  $V_c=3\text{m/min}$  and  $\gamma=0^\circ$  (respectively for the test made with  $V_c=3\text{m/min}$  and  $\gamma=15^\circ$ ). Images were chosen before the segment chip starts to slide with respect to the shear

plane (which corresponds to the final stage of the second phase (Fig. 14)) in order to avoid error on the computed strain fields induced by the crack propagation within the localized shear band and the segment sliding under the assumption of rigid body motion. Hence, the theory of the mechanics of continuum media is no longer valid for cumulative strain calculation during the third phase of segment chip formation. During Ti-6Al-4V chip segmentation, the shear strain cumulates at the tool tip and then propagates within the ASB [23, 24, 26]. Reaching the material failure, the crack starts to propagate from the tool tip towards the free surface of the workpiece. At this stage, the segment chip slides with respect to the shear plane under the assumption of rigid body motion. Results of the measured displacement fields are given in Figs. 15 and 16. The measured

**Fig. 16** a) Visual images obtained during Ti-6Al-4V segment chip formation under  $V_c=3\text{m/min}$  and  $\gamma=15^\circ$ ; b) displacement field along  $x$ -axis ( $U_x$ ) and c) displacement field along  $y$ -axis ( $U_y$ )



strain fields are given in Figs. 17 and 18. The displacement fields along  $x$ -axis (Figs. 15b and 16b) and  $y$ -axis (Figs. 15c and 16c) were obtained after conversion from pixel to micron unit.

- Analysis** Figures 15a and 16a give the visual images during Ti-6Al-4V segment chip formation as captured with the high-speed camera. It also gives the direction of the localized shear band. The cumulative displacement field along  $x$ -axis ( $U_x$ ) highlights a maximum gradient that reaches  $\approx 150\mu\text{m}$  during the final stage of the second phase of segment chip formation using  $0^\circ$  rake angle while it reaches  $\approx 130\mu\text{m}$  in the case using  $15^\circ$ . The gradient of the cumulative displacement field along  $y$ -axis ( $U_y$ ) is found also higher in the case using  $0^\circ$  rake angle than in the case using  $15^\circ$ . Therefore, segment chip is more subjected to deformation in the case using  $0^\circ$  rake angle. The measured strain fields (Figs. 17 and 18) highlight the appearance of localized shear band that is consistent with the mechanisms of Ti-6Al-4V chip formation. It shows that strains cumulated at the same location and there is no movement of the

shear plane during the first two phases of segment chip formation. Strain localization near the tool tip (phase 1) is shown to be slow and appears with image  $n^\circ 20$  for both rake angles. Propagation of the strain localization from the tool tip towards the free surface of the workpiece (phase 2) occurs rapidly and ends with image  $n^\circ 32$ . At the subsurface of the workpiece and far from the machined surface, the strain components were found equal to 0 which is consistent with the assumption of rigid body motion at this zone. With a cutting tool of  $0^\circ$  rake angle, the equivalent strain reaches  $\approx 4$  in the localized shear band while it reaches  $\approx 3$  with a cutting tool of  $15^\circ$  rake angle. Using  $0^\circ$  rake angle, the segment chip was found to be more subjected to compression and shear than in the case using a  $15^\circ$  rake angle. The last can be correlated with the measured cutting efforts (Table 1) where the cutting and the feed forces using  $0^\circ$  rake angle are higher than in the case using  $15^\circ$  rake angle.

- Accuracy assessment** The main source of errors in strain field measurement within the cutting zone is the

**Fig. 17** The measured Eulerian-Almansi strain components during Ti-6Al-4V chip segmentation under  $V_c=3\text{m/min}$  and  $\gamma=0^\circ$ : a)  $A_{xx}$ ; b)  $A_{xy}$ ; c)  $A_{yy}$  and d)  $A_{eq}$

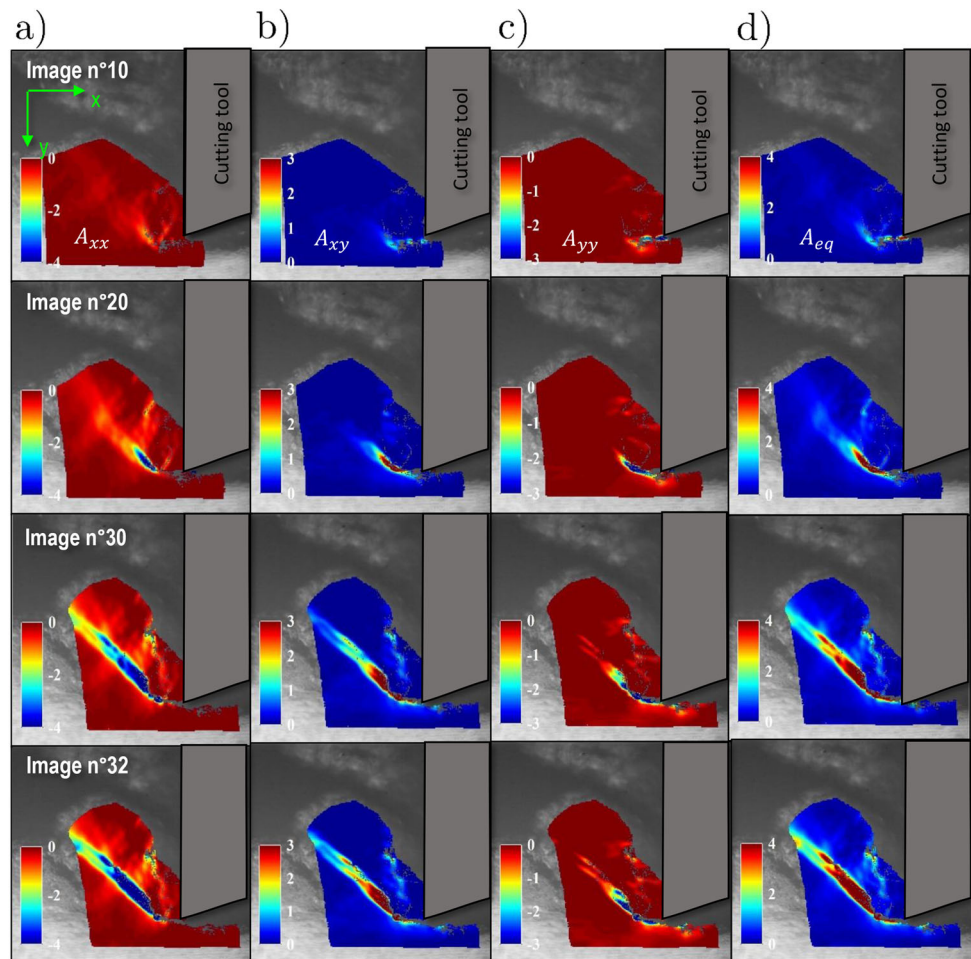
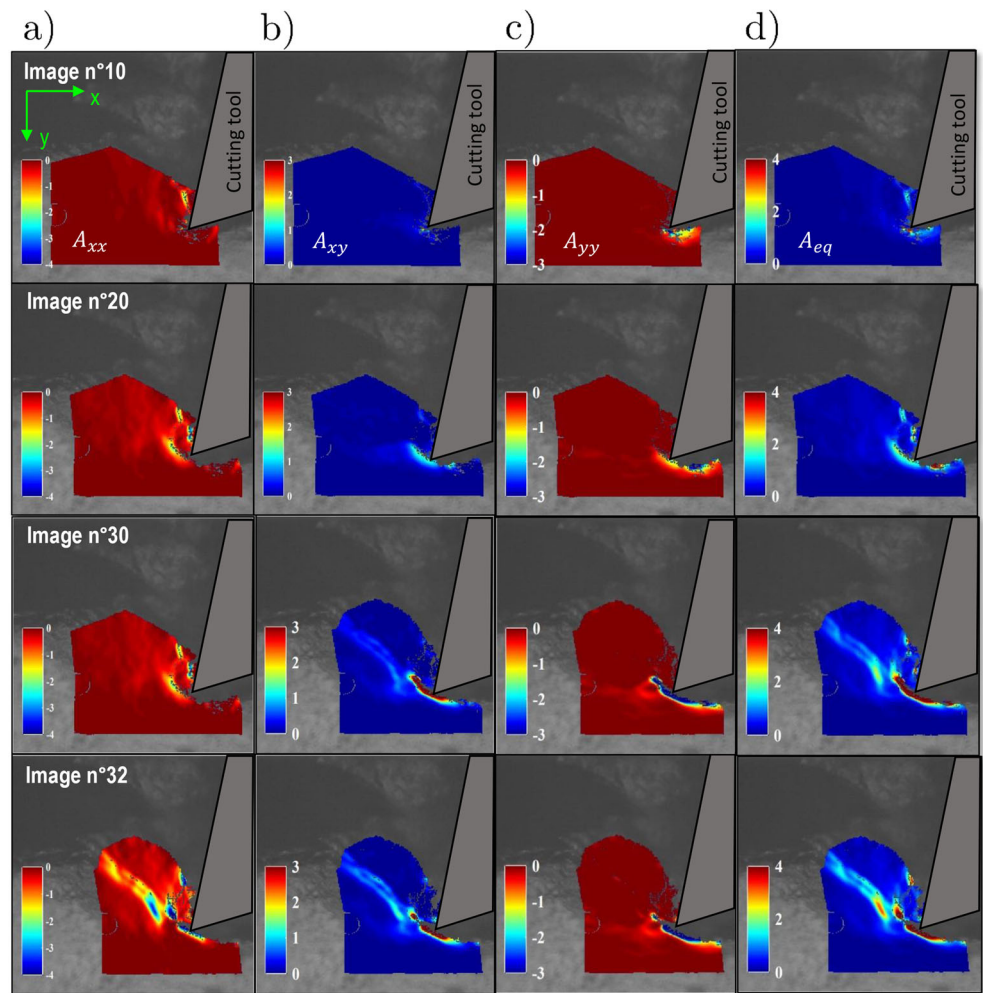


**Fig. 18** The measured Eulerian-Almansi strain components during Ti-6Al-4V chip segmentation under  $V_c=3\text{m/min}$  and  $\gamma=15^\circ$ : a)  $A_{xx}$ ; b)  $A_{xy}$ ; c)  $A_{yy}$  and d)  $A_{eq}$



out-of-plane motion of the chip. In order to evaluate the accuracy of the measured strain fields, the effect of out-of-plane displacement was examined. An out-of-plane displacement with an increment of  $10\mu\text{m}$  was applied along the optical axis and an image was recorded at each step. The mean value of the virtual equivalent strain was measured.

The result of the measured mean value of the virtual equivalent strain function of the out-of-plane displacement and for different subset radius is given in Fig. 19. Using a subset radius of 25pixels, the maximum mean value of the virtual equivalent strain reaches  $\approx 6, 5 \cdot 10^{-2}$  which is negligible comparing to the measured equivalent strain reached in the localized shear band ( $\approx 4$  using  $0^\circ$  rake angle and  $\approx 3$  using  $15^\circ$  rake angle). The last proves the property of the DIC application for kinematic fields measurement during orthogonal cutting and therefore reliability of the measured strain fields.

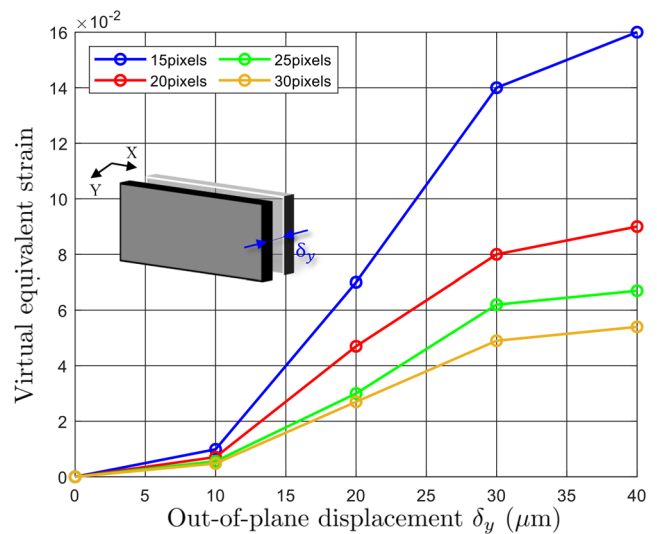


**Fig. 19** Mean value of the virtual equivalent strain function of the out-of-plane displacement and for different subset radius

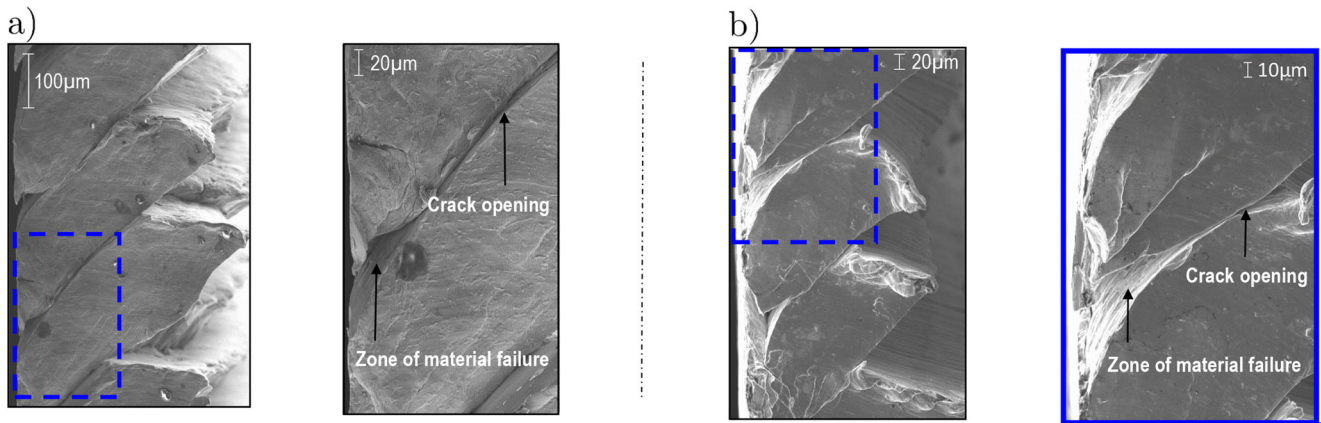


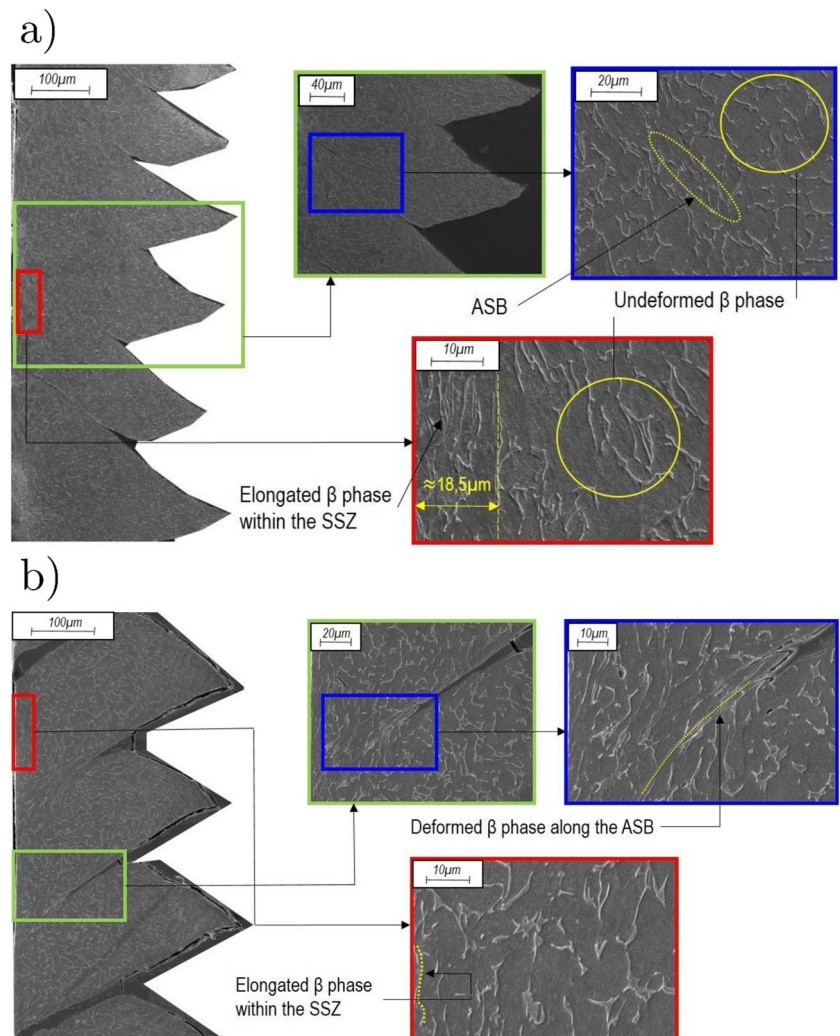
Fig. 20 SEM view on Ti-6Al-4V chip obtained during orthogonal cutting under  $V_c=3\text{m/min}$ : a)  $\gamma=0^\circ$  and b)  $\gamma=15^\circ$

### 6 Chip morphology and characteristic

- **Chip morphology analysis** A scanning electron microscopy (SEM) view was made on Ti-6Al-4V chip.

Segmented chips were observed highlighting crack opening within the localized shear band and high material failure near the tool-chip contact zone (Fig. 20). The last gives one of the main difficulties of the DIC

Fig. 21 Ti-6Al-4V chip microstructure obtained after orthogonal cutting under  $V_c=3\text{m/min}$ : a)  $\gamma=0^\circ$  and b)  $\gamma=15^\circ$



application in the context of kinematic fields measurement during orthogonal cutting. Material discontinuity induced by crack implies subset truncation for more accuracy in the measured strain fields.

- Chip microstructure analysis** Collected chips were polished and etched in order to study the impact of the cutting process on the material microstructure. SEM views (Fig. 21) were made on the Ti-6Al-4V chips. A focus was done on the primary and the secondary shear zones. A deformed  $\beta$ -phase was observed within the adiabatic shear band. Elongated  $\beta$ -phase was observed within the secondary shear zone (SSZ). The width of the SSZ in the case using  $0^\circ$  rake angle (Fig. 21a) is equal to  $18.5\mu\text{m}$ . Less elongated  $\beta$ -phase was observed in the SSZ when using a  $15^\circ$  rake angle (Fig. 21b). The last proves that material within the SSZ is more subjected to deformation in the case using  $0^\circ$  rake angle. Figure 21 shows crack near the free surface of the chip which is not connected to the tool-chip contact zone. Indeed, this observation is made through the width of the chip after material removal due to polishing. It highlights the difference between crack formation at the surface

of the chip (Fig. 20) and through the width (Fig. 21). As mentioned by Komanduri et al. [34] and proven by Pottier et al. [23] (after observation of the chip through thickness), this results from the high hydrostatic stress within the center of the chip which disables crack formation near the tool-chip contact zone.

- Segment width and shear angle analysis** The recorded video of the cutting process was obtained with sufficient quality allowing for the measurement of the segment width and the shear angle (Fig. 22). The segment width was measured in order study the effect of the rake angle on the chip compression.

Occurrence of the chip segment width was fitted with a normal distribution in order to determine the mean value of the chip segment width for both the tests. In the case using a  $0^\circ$  rake angle (Fig. 22a), the mean value of the chip segment width is equal to  $0.17\text{mm}$  which is slightly lower than in the case using  $15^\circ$  rake angle (Fig. 22b) as the mean value of the chip segment width was found equal to  $0.19\text{mm}$ . The last can be traced back to the fact that the chip segment is more subjected to compression along  $x$ - and  $y$ -axis ( $A_{xx}$  and  $A_{yy}$ ) in

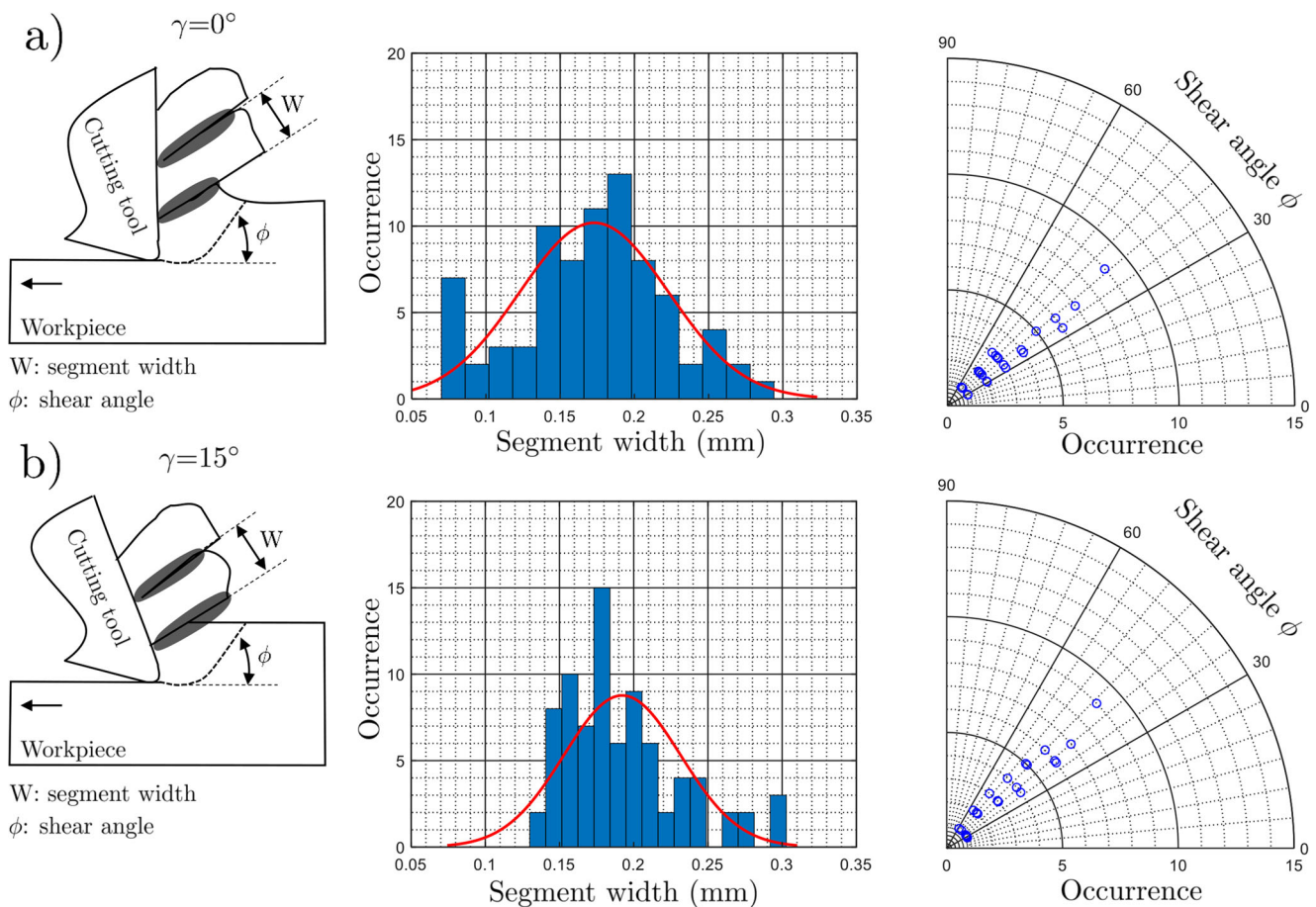


**Fig. 22** Ti-6Al-4V chip characteristics: occurrence of the chip segment width and the shear angle measured from the recorded video obtained during orthogonal cutting under  $V_c=3\text{m/min}$ : a)  $\gamma=0^\circ$  and b)  $\gamma=15^\circ$

the case using  $0^\circ$  rake angle (Fig. 17a and c) than in the case using  $15^\circ$  rake angle (Fig. 18a and c). The measured shear angle ranges almost between  $30$  and  $60^\circ$  for both rake angles. This proves the changes of the shear plane location in each segment chip formation. It can be associated to the difference of grain orientation. A significant dispersion on the measured segment width can be seen from Fig. 22. It may result from the difference of the thermomechanical load reached in the PSZ, responsible of the material failure. As a result, the amount of material failure will be different from one segment to another.

## 7 Conclusion

This paper outlines the methodology and technique used for kinematic fields measurement during orthogonal cutting and thus a local scale analysis of Ti-6Al-4V chip formation. In situ visualization of the material flow during chip formation remains a non-trivial task regarding the submillimetric size of the cutting zone and the rapidity of the orthogonal cutting process. New experimental bench was designed and used for instrumented orthogonal cutting tests. A dedicated optical system using beam-splitter for coaxial illumination that made possible to reveal the material microstructure considered as a natural speckle for particle tracking was proposed. An optical solution for intense illumination of submillimetric zone was designed and allows to reach a relatively high cutting speed of 40m/min. Unblurred images which are well exposed to light were obtained from the cutting zone. A novel method of DIC technique was applied on the recorded images and yields to measure the cumulative kinematic fields. It allows to study the evolution of the strain fields during one segment chip formation. The measured strain fields highlight the appearance of localized shear band which is consistent with the mechanisms of Ti-6Al-4V chip formation. Indeed, the segment chip was found to be subjected mainly to shear and compression. Moreover, at the subsurface of the workpiece and far from the machined surface, the measured strain fields was found equal to 0 which match with the assumption of rigid body motion at this zone. In order to evaluate the property of the DIC application, the effect of out-of-plane displacement was examined. The mean value of the virtual equivalent strain was found negligible compared to the measured equivalent strain reached in the localized shear band and thus proves the reliability of the measured strain fields. Correlation between the measured strain fields along  $x$ - and  $y$ -axis and the mean value of the chip segment width was made in order to reveal the effect of the cutting tool rake angle. Indeed, using a  $0^\circ$  rake angle, the chip segment was found to be more subjected to compression which explains

the fact that the mean value of the chip segment width is lower compared to the case using  $15^\circ$  rake angle. In future work, instrumented orthogonal cutting tests on Ti-6Al-4V will be conducted with higher cutting speeds. This require increasing the frame rate and the light intensity that leads to reduce the integration time in order to obtain good images qualities under cutting speeds that may be closer from the used ones in industry.

**Author contributions** Conceptualization, H.Z.; methodology, H.Z.; validation, M.C., V.W., O.C. and G.D.; investigation, H.Z.; writing—original draft, H.Z.; review and editing, M.C and V.W.; supervision, M.C., V.W., O.C. and G.D.; project administration, O.C and G.D. All authors have read and agreed to the published version of the manuscript.

**Funding** This project received funding from the European Union's Marie Skłodowska-Curie Actions (MSCA) Innovative Training Networks (ITN) H2020-MSCA-ITN-2017 under the grant agreement no. 764979.

## Declarations

**Competing interests** (Check journal-specific guidelines for which heading to use)

## References

1. Wagner V, Barelli F, Dessein G, Laheurte R, Darnis P, Cahuc O, Mousseigne M (2017) Comparison of the chip formations during turning of Ti64  $\beta$  and Ti64  $\alpha+\beta$ . *J Eng Manuf* 233:0954405417728309
2. Wagner V, Barelli F, Dessein G, Laheurte R, Darnis P, Cahuc O, Mousseigne M (2017) Thermal and microstructure study of the chip formation during turning of a lamellar titanium structure : the Ti64  $\beta$ . *J Manuf Sci Eng* 140:031010
3. Zhang XP, Shivpuri R, Srivastava AK (2014) Role of phase transformation in chip segmentation during high speed machining of dual phase titanium alloys. *J Mater Process Technol* 214:3048–3066
4. Melkote SN, Liu R, Fernandez-Zelaia P, Marusich T (2015) A physically based constitutive model for simulation of segmented chip formation in orthogonal cutting of commercially pure titanium. *CIRP Ann Manuf Technol* 64:65–68
5. Li A, Pang J, Zhao J, Zang J, Wang F (2017) FEM-simulation of machining induced surface plastic deformation and microstructural texture evolution of Ti-6Al-4V alloy. *Int J Mech Sci* 123:214–223
6. Huang Y, Ji J, Lee KM (2018) An improved material constitutive model considering temperature-dependent dynamic recrystallization for numerical analysis of Ti-6Al-4V alloy machining. *Int J Adv Manuf Technol* 97:3655–3670
7. Baizeau T, Campocasso S, Fromentin G, Besnard R (2017) Kinematic field measurements during orthogonal cutting tests via DIC with double-frame camera and pulsed laser lighting. *Exp Mech* 57:581–591
8. Yang ZH, Zhang XM, Nie GC, Zhang D, Ding H (2021) A comprehensive experiment-based approach to generate stress field and slip lines in cutting process. *J Manuf Sci Eng* 143:071014
9. Thimm B, Steden J, Reuber M, Christ HJ (2019) Using digital image correlation measurements for the inverse identification

- of constitutive material parameters applied in metal cutting simulations. In: Ozturk E (ed) 17th CIRP conference on modelling of machining operations, Sheffield, 13-14 June. United Kingdom, pp 95–100
10. Calamaz M, Coupard D, Girof F (2010) Numerical simulation of titanium alloy dry machining with a strain softening constitutive law. *Mach Sci Technol* 14:244–257
  11. Rotella G, Dillon O, Umbrello D, Settineri L, Jawahir I (2013) Finite element modeling of microstructural changes in turning of AA7075-t651 alloy. *J Manuf Process* 15:87–95
  12. Jafarian F, Ciaran MI, Umbrello D, Arrazola PJ, Filice L, Amirabadi H (2014) Finite element simulation of machining Inconel 718 alloy including microstructure changes. *Int J Mech Sci* 88:110–121
  13. Wang Q, Liu Z, Wang B, Song Q, Wan Y (2016) Evolutions of grain size and micro-hardness during chip formation and machined surface generation for Ti-6Al-4V in high-speed machining. *Int J Adv Manuf Technol* 82:1725–1736
  14. Battaglia JL, Puigsegur L, Cahuc O (2006) Estimated temperature on a machined surface using an inverse approach. *Experimental Heat Transfer* 18:13–32
  15. Cahuc O, Darnis P, Laheurte R (2007) Mechanical and thermal experiments in cutting process for new behaviour law. *Int J Form Process* 10:235–269
  16. Atlati S, Haddag B, Nouari M, Zenasni M (2014) Thermomechanical modelling of the tool–workmaterial interface in machining and its implementation using the ABAQUS VUINTER subroutine. *Int J Mech Sci* 87:102–117
  17. Haddag B, Atlati S, Nouari M, Zenasni M (2015) Analysis of the heat transfer at the tool–workpiece interface in machining: determination of heat generation and heat transfer coefficients. *Heat Mass Transfer* 51:1355–1370
  18. Hijazi A, Madhavan V (2008) A novel ultra-high speed camera for digital image processing applications. *Meas Sci Technol* 19:085503
  19. Pujana J, Arrazola PJ, Villar JA (2008) In-process high-speed photography applied to orthogonal turning. *Journal of materials processing technology* 202:475–485
  20. Ghadbeigi H, Bradbury SR, Pinna C, Yates JR (2008) Determination of micro-scale plastic strain caused by orthogonal cutting. *Int J Mach Tools Manuf* 45:228–235
  21. Bitans K, Brown RH (1965) TAn investigation of the deformation in orthogonal cutting. *International Journal of Machine Tool Design and Research* 5:155–165
  22. Vorm T (1976) Development of a quick-stop device and an analysis of the frozen-chip technique. *International Journal of Machine Tool Design and Research* 16:241–250
  23. Pottier T, Germain G, Calamaz M, Morel A, Coupard D (2014) Sub-Millimeter measurement of finite strains at cutting tool tip vicinity. *Experimental Mechanics* 54:1031–1042
  24. Harzallah M, Pottier T, Gilblas R, Landon Y, Mousseigne M, Senatore J (2018) A coupled in-situ measurement of temperature and kinematic fields in Ti-6Al-4V serrated chip formation at micro-scale. *Int J Mach Tools Manuf* 130-131:20–35
  25. Zhang D, Zhang XM, Xu WJ, Ding H (2017) Stress field analysis in orthogonal cutting process using digital image correlation technique. *J Manuf Sci Eng* 139:03100
  26. Davies B, Dabrow D, Ifju P, Xiao G, Liang SY, Huang Y (2018) Study of the shear strain and shear strain rate progression during titanium machining. *J Manuf Sci Eng* 140:051007
  27. Meurer M, Augspurger T, Tekkaya B, Schraknepper D, Lima AP, Bergs T (2020) Development of a methodology for strain field analysis during orthogonal cutting. In: Arrazola PJ (ed) 5th CIRP conference on surface integrity. Online, 1-5 June, pp 444-449
  28. Zouabi H, Calamaz M, Wagner V, Cahuc O, Dessein G (2021) Kinematic fields measurement during orthogonal cutting using digital images correlation: a review. *Journal of Manufacturing and Materials Processing* 5:1–23
  29. Calamaz M, Coupard D, Girof F (2012) Strain Field Measurement in Orthogonal Machining of a Titanium Alloy. *Journal of Advanced Materials Research* 498:237–242
  30. Hild F, Roux S (2008) Correli Q4: A Software for Finite Element Displacement Fields Measurement by Digital Image Correlation Internal Report N° 269. ENS de Cachan, France
  31. Vacher P, Dumoulin S, Morestin F, Mguil-Touchal S (1997) Bidimensional strain measurement using digital images. *J Mech Eng Sci* 213:811–817
  32. Blaber J, Adair B, Antoniou A (2015) Ncorr: open-source 2D digital image correlation MATLAB software. *Exp Mech* 55:1105–1122
  33. Pan B, Qian K, Xie H, Asundi A (2009) Two-dimensional digital image correlation for in-plane displacement and strain measurement: a review. *Meas Sci Technol* 20:062001
  34. Komanduri R, Von Turkovich BF (1981) New observations on the mechanisms of chip formation when machining titanium alloys. *Journal of Wear* 69:179–188

**Publisher's note** Springer Nature remains neutral with regard to jurisdictional claims in published maps and institutional affiliations.

Springer Nature or its licensor (e.g. a society or other partner) holds exclusive rights to this article under a publishing agreement with the author(s) or other rightsholder(s); author self-archiving of the accepted manuscript version of this article is solely governed by the terms of such publishing agreement and applicable law.